INVESTIGATING THE ROLE OF PHOTOEMISSION IN THE E-CLOUD FORMATION AT THE LHC

P. Dijkstal*, G. Iadarola†, L. Mether, G. Rumolo
CERN, CH-1211 Geneva 23, Switzerland

Abstract

The presence of electron clouds at the LHC gives rise to several problems, among them is the heat deposited by the electrons on the beam screens of the superconducting magnets, which constitutes a significant load for the cooling system. To improve the understanding of this phenomenon, simulation studies of the e-cloud build-up are performed using the dedicated simulation tool PyECLOUD. Photoelectrons generated by synchrotron radiation can significantly enhance the e-cloud formation. In this contribution, the available literature on photoelectric properties of the material used for the LHC beam screens is reviewed, and the number of photons emitted by the beam is calculated. This allows the definition of suitable simulation parameters for modeling the electrons from photoemission within the PyECLOUD code. The simulations with photoemission seeding are compared to those that neglect photoemitted electrons. The predicted heat loads are compared against measurements from LHC cryogenic cells. Since these cells include several kinds of magnets, simulations with different configurations of the externally applied magnetic field had to be combined. Furthermore a sensitivity study on the modeling of synchrotron radiation is presented.

INTRODUCTION

The formation of electron clouds in the arcs of the Large Hadron Collider (LHC) has been identified as one of the main limitations for the performance of the machine, especially when operating with the nominal bunch spacing of 25 ns [1–4].

Electron clouds can in particular induce severe beam degradation through beam losses, emittance growth and instabilities. Furthermore, the impacting electrons can deposit a significant power on the cold beam screens of the LHC superconducting magnets, which translates into a significant heat load for the cryogenic system. Heat load management will be even more critical in the HL-LHC era, also because the increased bunch intensity will entail a larger heat load from impedance and synchrotron radiation, reducing the available margin for e-cloud heat loads [5].

In order to understand in detail these effects and make reliable predictions for the future, we developed a detailed model of the e-cloud formation in the different elements of the LHC arc half-cell using the PyECLOUD simulation code [6, 7]. The model includes the main dipole and quadrupole magnets, shorter corrector magnets and drift spaces.

Particular care is taken to correctly model the impact of the photoelectrons. For this purpose, we reviewed the available literature on the characterization of the LHC beam screen surface in terms of reflectivity and photoelectron yield and we defined the necessary steps to obtain the photoemission model in the format required by the PyECLOUD code.

The number of photons that is capable of producing photoelectrons is calculated from basic electrodynamics equations. The photoelectric properties of the copper surface of the LHC beam screens have been measured at CERN and other laboratories, mainly in the late 90s and early 2000s [8–11]. The results are summarized and compared in this report, and the corresponding input parameters for PyECLOUD are defined.

Simulations of the magnetic elements that are part of the cryogenic cell of the LHC arcs, such as dipoles, quadrupoles and drift spaces, were performed. In this contribution, the estimated heat loads are compared to measurements collected during LHC operation. The impact of the photoelectrons on the simulation results is investigated. More information about these studies can be found in [12].

EMISSION OF PHOTOELECTRONS FROM THE LHC BEAM SCREENS

Photons are generated by the beam that follows a curved trajectory within dipole magnets. These photons hit the beam chamber surfaces where they are eventually absorbed, possibly after being reflected once or multiple times. We analyze this problem in several steps to finally obtain the model parameters required for e-cloud simulation studies.

Emission of photons by a proton beam in the LHC

The amount of photons generated by a proton having a relativistic parameter γ_{rel} and following a circular trajectory with bending radius ρ has to be calculated. The problem can be solved analytically following the treatment explained in [14].

The following equation describes the power spectrum $\frac{\mathrm{d}P}{\mathrm{d}\omega}$ of the radiation emitted by a highly relativistic charged particle ($\beta_{\mathrm{rel}} \approx 1$) on a circular trajectory:

$$\frac{\mathrm{d}P}{\mathrm{d}\omega} = \frac{P_s}{\omega_c} S_s \left(\frac{\omega}{\omega_c} \right) \tag{1}$$

* Current address: Paul Scherrer Institut, CH-5232 Villigen PSI, Switzerland
† Correspondence e-mail: giovanni.iadarola@cern.ch

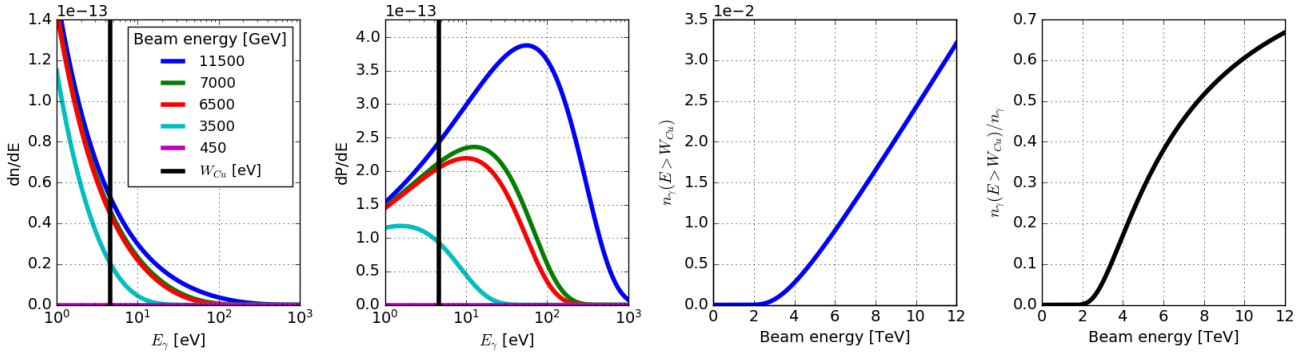

Figure 1: Left: the photon energy distribution of the synchrotron radiation emitted by a proton travelling in an LHC dipole with different kinetic energies. Middle left: the corresponding emitted power spectrum. Middle right: the number of photons above the work function of copper W_{Cu} (4.6 eV [13]) as a function of the proton energy. Right: the fraction of photons with an energy above W_{Cu} as a function of the proton energy.

where P_s is the total emitted power,

$$P_s = \frac{e^2}{4\pi\epsilon_0}\frac{2c\gamma_{\mathrm{rel}}^4}{3\rho^2} \tag{2}$$

and ω_c the critical frequency of the radiation:

$$\omega_c = \frac{E_c}{\hbar} = \frac{3c\gamma_{\mathrm{rel}}^3}{2\rho} \tag{3}$$

The function S_s is an integral of the modified Bessel function $K_{5/3}$:

$$S_s(x) = \frac{9\sqrt{3}}{8\pi}x\int_x^\infty K_{5/3}(z)\mathrm{d}z \tag{4}$$

The photon energy is related to the radiation frequency by:

$$E_\gamma(\omega) = \hbar\omega \tag{5}$$

The emitted power spectrum is related to the spectrum of emitted photons per unit time $\frac{\mathrm{d}\dot{n}_\gamma}{\mathrm{d}\omega}$:

$$\frac{\mathrm{d}P}{\mathrm{d}\omega} = \hbar\omega\frac{\mathrm{d}\dot{n}_\gamma}{\mathrm{d}\omega} \tag{6}$$

Using Eq. 1 we obtain:

$$\frac{\mathrm{d}\dot{n}_\gamma}{\mathrm{d}\omega} = \frac{1}{\hbar\omega}\frac{\mathrm{d}P}{\mathrm{d}\omega} = \frac{1}{\hbar\omega}\frac{P_s}{\omega_c}S_s\left(\frac{\omega}{\omega_c}\right) \tag{7}$$

Figure 1 shows the photon spectrum in Eq. 7 as a function of the photon energy for different energies of the LHC proton beam, together with the corresponding power spectrum of the radiation.

The number of photons above a certain frequency per unit path length is given by (see [12]):

$$n_\gamma(\omega > \omega_{\mathrm{min}}) = \frac{\sqrt{3}}{8\pi^2}\frac{e^2\gamma_{\mathrm{rel}}}{\hbar c\epsilon_0\rho}\cdot\int_{\frac{\omega_{\mathrm{min}}}{\omega_c}}^\infty K_{5/3}(x)\left(x-\frac{\omega_{\mathrm{min}}}{\omega_c}\right)\mathrm{d}x \tag{8}$$

Note that also ω_c depends on γ_{rel}, with the effect that $n_\gamma(\omega > \omega_{\mathrm{min}})$ depends non-linearly on the beam energy as shown in Fig. 1.

Due to the photoelectric effect, electrons can be extracted from the beam chamber surface. The work function of a metal is the energy gap between the Fermi and vacuum energy levels, which is 4.6 eV in the case of copper [13], the material of the LHC beam screen surface. Only photons with energy sufficient to overcome this gap can contribute to the photoelectron generation process. The plots in Fig. 1 show the number of such photons per unit length and per proton, as well as their ratio with respect to all photons.

Another interesting feature is the angular distribution of photons. Far above the critical angle θ_c, emission of synchrotron radiation is negligible. The critical angle can be written as:

$$\theta_c(\omega) = \frac{1}{\gamma_{\mathrm{rel}}}\left(\frac{2\omega_c}{\omega}\right)^{1/3} = \left(\frac{3c}{\rho\omega}\right)^{1/3} \tag{9}$$

For energies corresponding to the copper work function, the critical angle is about 0.36 mrad. It is even smaller for higher energies.

Beam screen photoemission properties from past measurement campaigns

The beam screen that is installed in the cryogenic magnets of the LHC has the purpose of absorbing the heat load caused by the beam through impedance, synchrotron radiation and electron cloud effects. This beam screen is made of stainless steel with a surface of co-laminated copper. It is thermally isolated from the liquid helium and kept at a temperature between 4.6 and 20 K, which allows for more efficient cooling compared to 1.9 K, the temperature of the superconducting coils of the magnets [15]. The beam screen is cooled by a flow of weakly supercritical helium through two small attached tubes (see Fig. 2) and is perforated to enable the vacuum pumping of the volume inside. The pumping slots are covered by shields that intercept electrons before they can reach the cold bore [16].

The majority of the beam screens at the LHC are installed within strong dipolar magnetic fields. Photoelectrons generated at the side of the chamber are confined there by the magnetic field and cannot move to the center of the pipe where the beam is located. Compared to those electrons that are generated at the top and bottom parts of the beam chamber, they receive a much weaker kick from the beam in the direction in which they are free to move, and therefore have a limited impact on heat loads and beam stability.

For these reasons, at the side of the beam screen that is exposed to direct synchrotron radiation, the surface exhibits a sawtooth structure (Fig. 2 - bottom). Its purpose is to avoid a grazing impact of the photons and thereby provide a smaller probability of reflection. This results in a large fraction of photoelectrons being generated at the side of the chamber where they are less harmful.

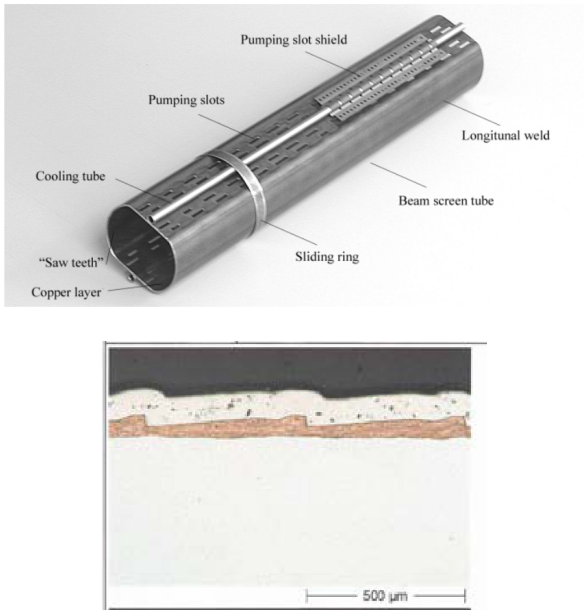

Figure 2: Top: the beam screen used at the LHC [16]. Bottom: the sawtooth structure present on the side where the synchrotron radiation first impacts, in order to have a low probability of photon reflection [17].

Photoemission from the LHC beam screens was extensively studied with dedicated measurements between 1998 and 2004 [8–11]. The present section summarizes the main results of these studies that are relevant for the simulation of the electron cloud formation in the LHC arcs. The following notation is used in most of them: R is the photon reflectivity of the material, and Y, Y^* are respectively the photoelectron yields per incident and absorbed photon. They are defined as follows, where N_e and n_γ are the number of photoelectrons and the number of photons, respectively:

$$n_{\gamma,\text{incident}} = n_{\gamma,\text{absorbed}} + n_{\gamma,\text{reflected}} \tag{10}$$

$$R = \frac{n_{\gamma,\text{reflected}}}{n_{\gamma,\text{incident}}} \tag{11}$$

$$Y = \frac{N_e}{n_{\gamma,\text{incident}}} \tag{12}$$

$$Y^* = \frac{N_e}{n_{\gamma,\text{absorbed}}} = \frac{Y}{1-R} \tag{13}$$

Table 1: Photoemission properties for different materials when irradiated by synchrotron radiation with different critical photon energy [8].

		45 eV		194 eV	
Surface	Status	R (%)	Y* (e/ph)	R (%)	Y* (e/ph)
Cu co-lam.	as-received	80.9	0.114	77.0	0.318
	air baked	21.7	0.096	18.2	0.180
Cu elect.	as-received	5.0	0.084	6.9	0.078
Cu sawtooth	as-received	1.8	0.053	-	-
	150°C, 9h	1.3	0.053	1.2	0.052
	150°C, 24h	1.3	0.040	1.2	0.040

In [8], the properties of several materials were studied using synchrotron radiation from the EPA ring, including co-laminated copper with and without the sawtooth structure. It was possible to measure the reflectivity R (only in the forward direction), as well as the photoelectron yield Y^*. The main results of this article are provided in Table 1.

	45 eV		**194 eV**	
Dose (ph/m)	R (%)	Y* (e/ph)	R (%)	Y* (e/ph)
~ 2 10^{19}	8	0.029	7	0.040
1.5 10^{22}		0.015		0.022

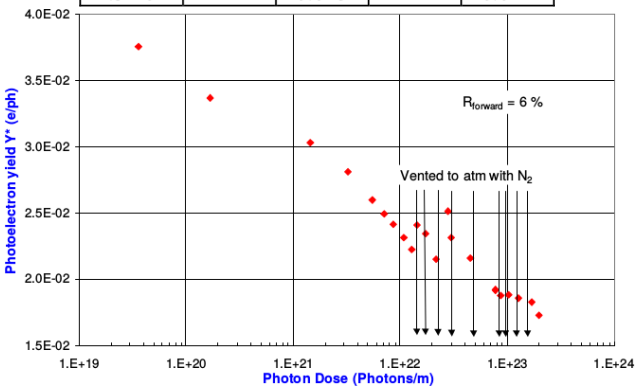

Figure 3: Top: reflectivity and photoelectron yield from measurements of copper samples with sawtooth structure on the surface. Bottom: the impact of photon-induced conditioning on the photoelectron yield. Both results were published in [9].

A different experiment [9] quantified the effect of photon-induced conditioning ("scrubbing") on the photoelectron yield of co-laminated copper with sawtooth. Figure 3 shows

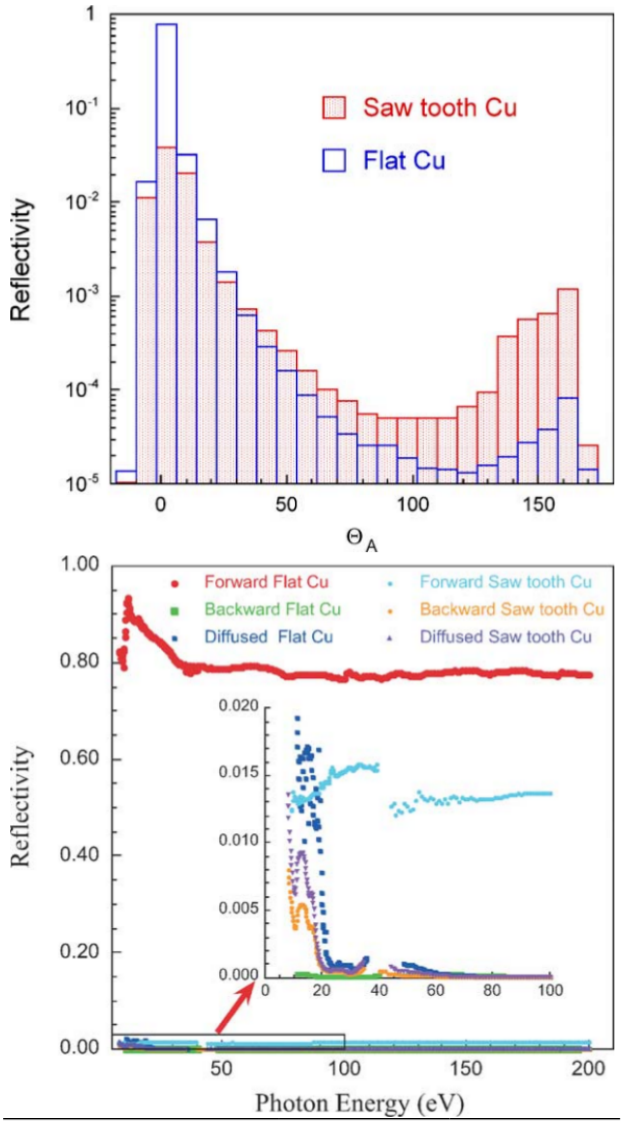

	Flat sample	Saw-tooth sample
Forward scattering (%)	80	4
Back scattering (%)	0	2
Diffused (%)	2	4
Total	82	10

Figure 4: Top: Measured reflectivity of Cu samples for different angles with respect to grazing incidence. Middle: Measured reflectivities for different photon energies and material configurations. Bottom: Summary of reflectivities for LHC-type photon spectrum. These results were published in [10].

the results. Photon "scrubbing" with a dose of $1.5 \cdot 10^{22}$ photons, corresponding to about 600 hours of nominal LHC operation, caused a decrease of the photoelectron yield by roughly 50%. The results indicate that this process had not saturated and that the yield could possibly have decreased even further with additional photon dose. No effect of photon "scrubbing" is observed on the photon reflectivities. One can note that this experiment measured larger photon reflectivities with respect to the results reported in [8].

The angular distribution of the reflected photons is studied in detail in [10]. Copper samples with and without sawtooth structures were irradiated with synchrotron light between 8 eV and 200 eV, and the reflectivities in different directions were measured. The main results of this article are shown in Fig. 4. The reflectivity as a function of the angle is shown for synchrotron radiation with a critical energy of 44 eV. In addition, the measured total reflectivity as a function of the photon energy is provided. In case of the sawtooth, the reflectivity is reported as 10%, which is larger than in [8] and [9] (1.8% and 8%, respectively). It was also found that R depends on the photon energy.

The comprehensive paper [11] covers many photoemission properties of different materials. Among these are the kinetic energy spectra of photoelectrons, the angular spectra of photoemission and the dependency of photoelectron yields on photon energy (see also Fig. 12). Furthermore, also the total photoemission yields and how these are affected by photon-induced conditioning are reported (see Table 2). Copper is among the studied materials, although only without a sawtooth-shaped surface. One has to note that, unlike in the previously mentioned measurement campaigns, the reflectivities were not measured. The photoelectron yields therefore correspond to yield per incident photon Y. It is notable that these tend to be higher than those presented in [8, 9]. However, the incident angle of photons was 45°, compared to a 11 mrad grazing incidence in case of [8, 9].

Parameters for photoemission simulations

In this section we will use the calculations and measurement results presented in the previous sections to model the generation of photoelectrons in PyECLOUD build-up simulations. For this purpose, we will use the notation defined in Tab. 3.

The PyECLOUD code [18] does not model photons directly. Instead, the photoemission process is described through the number of photoelectrons emitted per proton and per meter (**k_pe_st**), and the fraction of photoelectrons (**refl_frac**) not emitted from a narrow region in one specific part of the chamber, which corresponds to photons that are reflected at least once. This means that the quantity (1-**refl_frac**) is the fraction of photoelectrons generated at the part of the beam screen where the synchrotron radiation first impacts. The calculation of **k_pe_st** requires knowledge of the beam energy, since the number of photons with sufficient energy to generate photoelectrons ($n_\gamma(E > W_{\mathrm{Cu}})$) depends on the beam energy (see Eq. 8). In the following, $n_\gamma(E > W_{\mathrm{Cu}})$ is computed for the operational LHC beam energy, which is 6.5 TeV.

In the case of a uniform beam pipe surface, **k_pe_st** is simply computed as follows:

$$\mathbf{k\_pe\_st} = n_\gamma(E > W_{\mathrm{Cu}})Y^* \tag{14}$$

The reflection coefficient is not needed since all photons are eventually absorbed, either on direct impact or after an arbitrary number of reflections.

Table 2: Measured white light (WL) photoelectron yields for Au and Cu [11] before (low dose WL yield) and after (WL yield) conditioning with synchrotron radiation with a spectrum similar to that emitted by LHC beams. The yield decreased by about 40% as a consequence of this conditioning. The other columns that are labeled "energy window" only take into account those electrons that have been emitted with a kinetic energy between 1 and 6 eV.

Sample	Low dose WL yield (electrons/photon)	Energy window low dose WL yield (electrons/photon)	WL yield (electrons/photon)	Energy window WL yield (electrons/photon)
Au	0.047 ± 0.020	0.022 ± 0.020	0.041 ± 0.002	0.023 ± 0.002
Cu	0.103 ± 0.020	0.051 ± 0.020	0.063 ± 0.002	0.042 ± 0.002

Table 3: The notation used to describe the surface materials.

Y_i, Y_i^*	Photoelectron yields per incident and per absorbed electron (defined by Eq. 12 and Eq. 13) in the region of direct impact of the synchrotron radiation (i.e. sawtooth region)
Y_r, Y_r^*	Photoelectron yields per incident and per absorbed electron in the remaining part of the chamber
R_i, R_r	Reflection rates in the region of direct synchrotron radiation impact and in the remaining part of the chamber
N_i, N_r	Photoelectrons emitted in the region of direct impact of the synchrotron radiation and in the remaining part of the chamber
N_t	Total number of emitted photoelectrons
$n_\gamma(E > W_{\mathrm{Cu}})$	Number of photons with an energy above the copper work function, emitted per proton and per m in the LHC arc bending magnets (Eq. 8)

However, if the region of initial impact has special properties, e.g. the LHC beam screen with its sawtooth structure, the properties of both surface types must be taken into account. The photon numbers that are absorbed at the sawtooth part and after initial reflection are weighted with the respective photoelectron yields Y^* and the probability of initial reflection:

$$\begin{aligned} \textbf{k\_pe\_st} &= N_i + N_r && (15)\\ &= n_\gamma(E > W_{\mathrm{Cu}}) \left((1 - R_i)Y_i^* + R_i Y_r^*\right) && (16)\\ &= n_\gamma(E > W_{\mathrm{Cu}}) \left(Y_i + R_i Y_r^*\right) && (17) \end{aligned}$$

Here we ignore the effect of photons that are reflected back to the sawtooth material, as it covers only a small fraction of the total beam screen surface.

The quantity **refl_frac** is computed as follows:

$$\textbf{refl\_frac} = \frac{N_r}{N_t} = \frac{N_r}{N_i + N_r} = \frac{R_i Y_r^*}{(1 - R_i)Y_i^* + R_i Y_r^*} \quad (18)$$

Table 4 provides an overview of the results from the papers reviewed in the previous section. Y was not specified in [11] but can be calculated from Y^* and R. Since only the references [8, 9] include results for sawtooth materials, these publications are used to extract the parameters for electron cloud simulations. The reflectivities from [10] are chosen as they also include backward scattering of photons. The parameters (**refl_frac**) and (**k_pe_st**) are thus calculated from a combination of quantities that are not part of the same publication.

Two types of beam screens are considered, one with a sawtooth structure at the location where the synchrotron radiation directly impacts and another one with flat copper everywhere. The effect of photon-induced conditioning was not studied in each reference publication.

For a **conservative estimate** (Tab. 5), we do not take into account possible conditioning of the surfaces and we use the high photoelectron yields Y from [8].

An **optimistic estimate** (Tab. 6) includes the lowest yields that can be obtained from the published results that were summarized in the previous section. Photon conditioning effects need to be included for both the material in the sawtooth and elsewhere. This is quantified in [8, 9] for copper with sawtooth structures, in which case a reduction of the yield by a factor of 4.7 was observed ($Y = 0.052$ was measured in [8] before conditioning and $Y = 0.011$ was measured in [9] after conditioning). In the absence of published measurement results for smooth Cu after photon "scrubbing", we apply the same factor as for the sawtooth material, obtaining for the surface after conditioning: $Y = \frac{2.2 \cdot 10^{-2}}{4.7} = 4.6 \cdot 10^{-3}$.

Here the beam energy is only considered in the calculation of n_γ (Eq. 8). It shall be noted that the references [8–11] all used a synchrotron radiation spectrum that is very similar to the one from the LHC running at 7 TeV. In the absence of data that corresponds to a LHC at 6.5 TeV, we resort to using the available results for 7 TeV. However one should note that results corresponding to a 11.5 TeV beam (see Fig. **??** and 4) are significantly different from those corresponding to a 7 TeV beam.

Table 4: Different published experimental results on photoelectron yields and reflectivities. If two values are stated for a photoelectron yield, they correspond to measurements before and after photon "scrubbing". All other values are measured before photon conditioning. The reflectivities colored in red only include the forward reflectivity. The yields in blue were not published but could be retrieved with the simple relation between R, Y and Y^* (Eq. 13).

Source	Cu co-lam.			with sawtooth		
	R [%]	Y	Y^*	R [%]	Y	Y^*
Baglin et al. 1998 [8]	80.9	0.022	0.114	1.8	0.052	0.053
Cimino et al. 1999 [11]	-	0.103/0.063	-	-	-	-
Baglin et al. 2001 [9]	-	-	-	8	0.021/0.011	0.029/0.015
Mahne et al. 2004 [10]	82	-	-	10	-	-

Table 5: The yields and reflectivities from Tab. 4, together with the number of photons from Eq. 8, lead to a **conservative estimate** of the PyECLOUD input parameters refl_frac and k_pe_st.

Chamber type	R_i	R_r	Y_i	Y_r	Y_i^*	Y_r^*
Cu co-lam. with sawtooth	10.0	82.0	5.2e-02	2.2e-02	5.8e-02	1.2e-01
Cu co-lam.	82.0	82.0	2.3e-02	2.3e-02	1.3e-01	1.3e-01

Chamber type	N_i	N_r	N_t	n_γ	refl_frac	k_pe_st
Cu co-lam. with sawtooth	5.2e-02	1.2e-02	6.4e-02	1.1e-02	1.89e-01	7.00e-04
Cu co-lam.	2.3e-02	1.0e-01	1.3e-01	1.1e-02	8.20e-01	1.38e-03

Table 6: Photon "scrubbing" effects are considered to arrive at a more **optimistic estimate** with lower electron yields with respect to the values in Tab. 5.

Chamber type	R_i	R_r	Y_i	Y_r	Y_i^*	Y_r^*
Cu co-lam. with sawtooth	10.0	82.0	1.0e-02	4.6e-03	1.1e-02	2.6e-02
Cu co-lam.	82.0	82.0	4.6e-03	4.6e-03	2.6e-02	2.6e-02

Chamber type	N_i	N_r	N_t	n_γ	refl_frac	k_pe_st
Cu co-lam. with sawtooth	1.0e-02	2.6e-03	1.3e-02	1.1e-02	2.03e-01	1.39e-04
Cu co-lam.	4.6e-03	2.1e-02	2.6e-02	1.1e-02	8.20e-01	2.81e-04

PYECLOUD SIMULATIONS AND COMPARISON AGAINST HEAT LOAD MEASUREMENTS

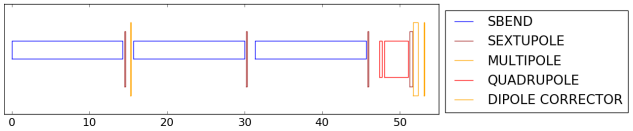

Figure 5: All cryogenic cells (half-cells in terms of beam optics) in the LHC arcs contain three main dipoles and one main quadrupole, interleaved by corrector magnets in different configurations. In this plot, one of the most common types of half-cells is sketched, showing only the magnetic elements.

The arcs of the LHC are divided in cryogenic cells, each of which contains three main dipoles, a main quadrupole and several corrector magnets, as shown in Fig. 5. Because two cryogenic cells correspond to a FODO cell in terms of beam optics, these are often called half-cells. The beam screen inside each of these cryogenic cells is cooled by a flow of weakly supercritical helium. Pressures and temperatures of the helium are measured at different points in each cell and allow a computation of the heat loads deposited on the corresponding beam screen [15]. The contributions of impedance and synchrotron radiation can be estimated starting from measured beam properties [19]. The remaining heat loads are attributed to electron cloud effects.

In this section, this heat load is compared to predictions based on electron cloud simulation results obtained with the PyECLOUD code. During such simulations, the cloud is modeled with macroparticles that are tracked through the electro-magnetic fields from three sources: the beam, the space-charge of the cloud itself and externally applied magnetic fields. Whenever particles hit the surface of the beam pipe, the multipacting process model [6] is sumulated. Furthermore, the impact energy is recorded. The main parameter of the secondary emission model is the SEY parameter. Snapshots of the electron distributions in various magnetic elements are shown in Fig. 6.

Simulation studies

PyECLOUD build-up simulation studies have been performed for all relevant magnetic elements and for the drift sections of the LHC arcs. Each of these magnets is simulated either with photoemission seeding or starting with a uniform initial distribution of 10^7 electrons per meter. Such an initial population is small with respect to the densities that are reached in simulations above the multipacting threshold.

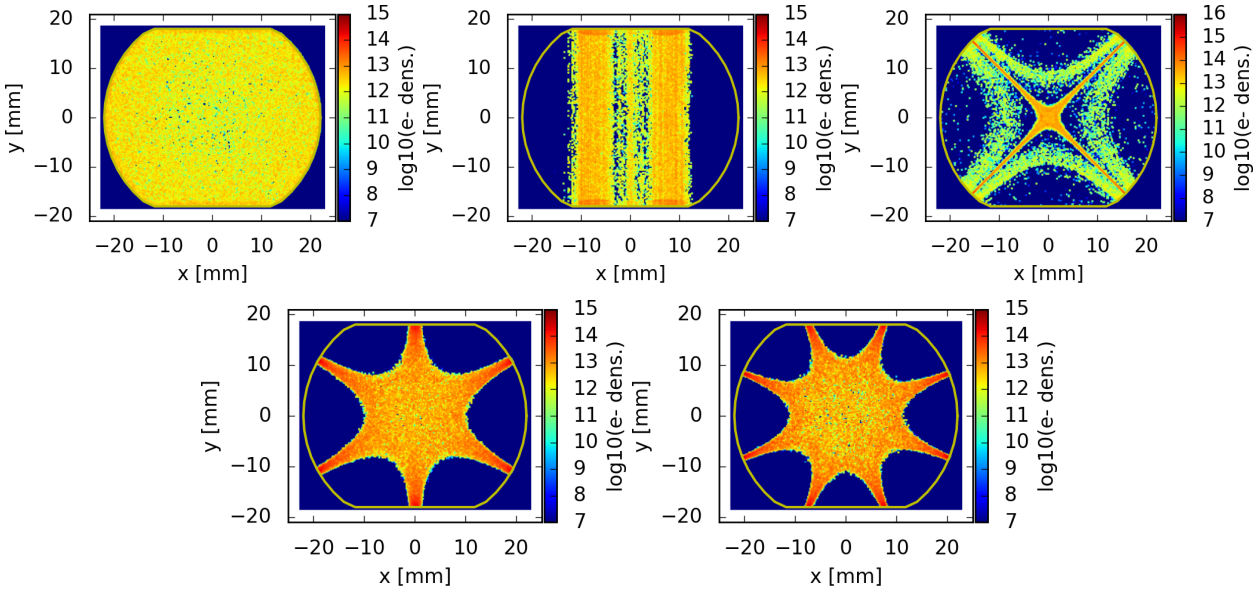

Figure 6: Electron density distributions of drifts, dipoles, quadrupoles, sextupoles and octupoles as obtained from PyECLOUD simulations.

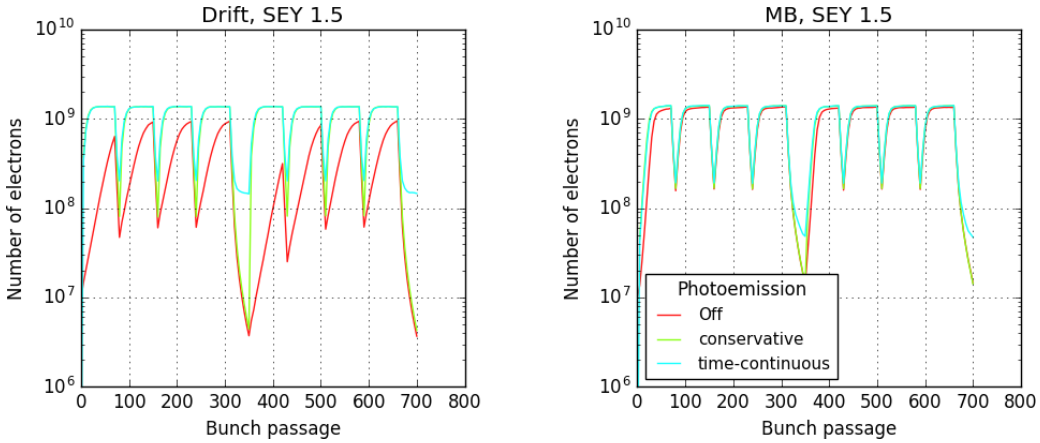

Figure 7: The evolution of the number of electrons per meter in the chamber of a drift and a dipole as obtained from PyECLOUD simulations with an SEY parameter of 1.2. The different electron cloud seeding mechanisms are compared.

The magnetic lengths and the operational magnetic field parameters of the simulated devices operating at a beam energy of 6.5 TeV are shown in Tab. 7. The length of a single magnet is given in the first column. There is no cell that contains all corrector magnets at once. The average length per half cell was found by taking all cryogenic cells in the arcs into account.

For all considered magnetic elements, simulations have been performed. The simulated beam consists of two trains of 288 bunches, each formed by four batches which in turn consist of 72 bunches. The two trains are interleaved with 30 empty bunch slots, and the consecutive batches are interleaved with eight empty slots. The heat load from the second train is rescaled in order to obtain the heat load that corresponds to a filled LHC machine with 2800 bunches in total, without having to simulate each train. This procedure is chosen since the electron cloud in the second and later trains are identical in case the electron density is saturated by the end of the train, a condition that is usually satisfied as shown in Fig. 7. The bunch intensity is set to $1.1{\cdot}10^{11}$ p/bunch.

Figure 8 shows heat loads as a function of the SEY parameter for different external magnetic field configurations. Simulations performed with and without photoelectrons are compared. A significant difference between the two is observed only for the drift spaces, and for the dipole magnets. In these cases both the conservative and optimistic photoemission parameters (as defined in Tabs. 5 and 6 respectively) have been simulated.

The multipacting threshold is significantly altered by the photoelectrons in the case of the drift space and of the vertical dipole corrector (MCBV). In these particular cases the photoelectrons generated by the direct impact of the synchrotron radiation at the side of the beam screen are not trapped by the magnetic field lines and can directly contribute to the multi-

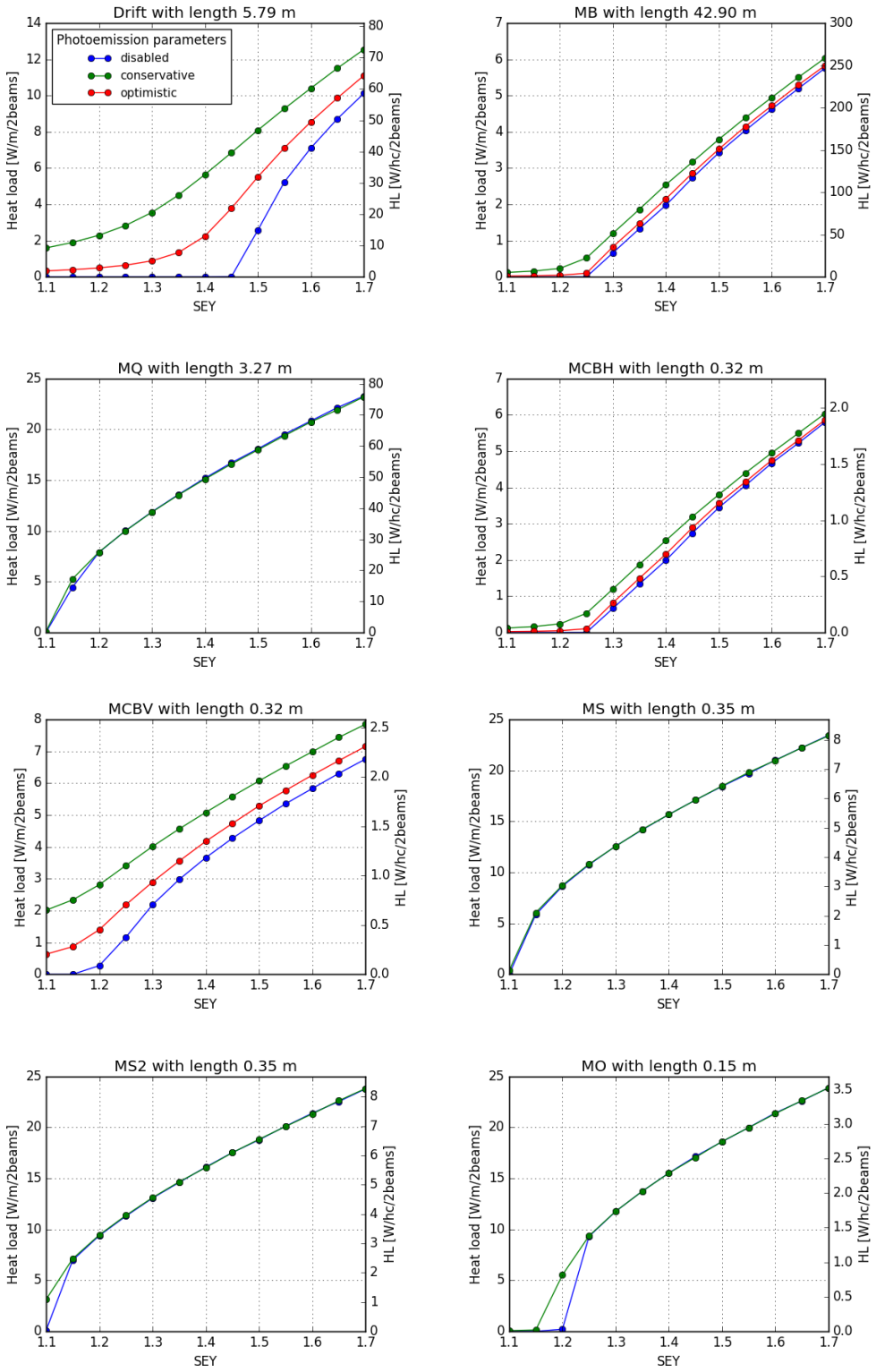

Figure 8: Heat loads from PyECLOUD simulationswithout photoelectron emission and with "conservative" photoemission parameters. In the case of the drifts and dipole magnets (MB, MCBH, MCBV), also the "optimistic" parameters have been simulated. The left axes correspond to the heat load per meter, the right axes to the heat load in the average cryogenic cell.

Table 7: Magnetic field strengths and gradients used in the simulation study. The lengths correspond to the average cryogenic cell in the LHC arcs.

Magnet	**Length per half cell** [m]	**Magnetic field**	**Skew mag. field**
Drift	5.79	-	-
Main Bend (MB)	42.90	7.73 T	-
Horizontal corrector (MCBH)	0.32	2.72 T	-
Vertical corrector (MCBV)	0.32	-	2.32 T
Main quadrupole (MQ)	3.27	$1.75{\cdot}10^2$ T/m	-
Main sextupole (MS)	0.35	$1.52{\cdot}10^3$ T/m^2	-
Main sextupole (MS2)	0.35	$-2.60{\cdot}10^3$ T/m^2	-
Main octupole (MO)	0.15	$3.47{\cdot}10^5$ T/m^3	-

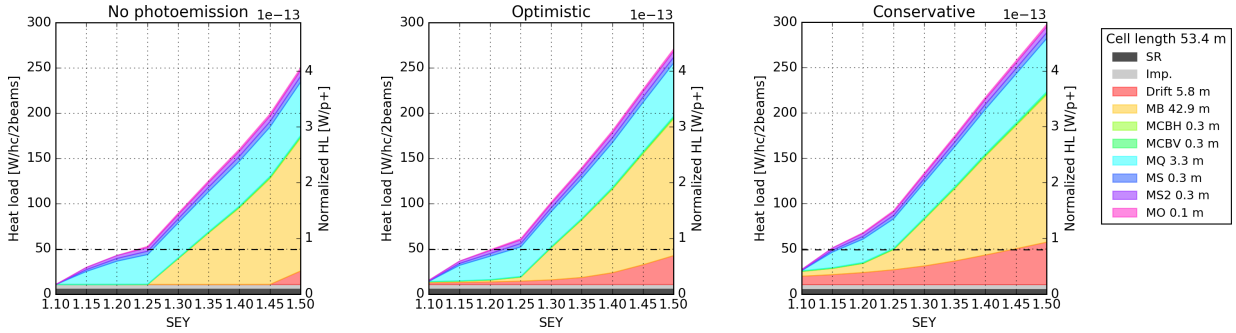

Figure 9: Total heat load in the average LHC half cell as a function of the SEY parameter of the beam-screen surface (assumed to be the same over the entire half-cell). The different contributions are shown in different colors. Three configurations for the photoemission are considered as indicated on top of the plots. The horizontal dashed line corresponds to the value measured in low heat load cells.

pacting. For all other magnet types, only the photoelectrons generated by reflected photons can contribute significantly (see Fig. 6) .

Comparison to the measured heat loads in the LHC

For each of the LHC arc half-cells the heat load deposited on the beam screens can be estimated from the measured thermodynamic parameters of the cooling fluid (e.g. temperatures, pressures). For standard arc cells, the installed sensors only allow measuring the total heat load over the two beam screens of the 53-m long half-cell, hence it is not possible to disentangle the effect of the single magnets nor of a single beam.

In order to compare these data with the simulations presented in the previous section, we have calculated the total heat load expected for the average arc half-cell, summing up the calculated contributions from impedance and synchrotron radiation [19] and the simulated e-cloud contribution from the different elements. This is done by assuming that all beam screen surfaces in the half-cell exhibit the same SEY parameter. As before, three configurations for the photoemission are considered: uniform initial seeding with no photoemission, conservative and optimistic surface parameters as described in the previous section. The results are shown in Fig. 9. The dashed lines indicate the heat load measured in a low-load cryogenic cell during a typical LHC fill [12, 20].

SENSITIVITY OF PHOTOEMISSION MODELING

Photoelectron yields and reflectivities are only a part of the information needed to model the effect of photoelectron seeding on the electron cloud build-up simulations. In this section we investigate the impact of the more implicit properties of the photoemission modeling. Changes to the simulation code have been introduced that vary the initial energy of photoelectrons and the times and locations at which they are generated in the chamber. The influence of these changes on the simulations is presented in the following subsections. More information can be founds in [12].

Delayed photoelectron production

In PyECLOUD, photoelectrons are generated with the same time structure as the longitudinal beam profile. In reality however, the two are not exactly synchronized due to the fact that the protons are bent by the magnetic field while the photons are not, as illustrated in Fig. 10. The difference is calculated in the following equations the bending radius (R) of the LHC main dipoles is 2803.9 m and the radius of the chamber (r) is 22 mm). A beam travelling at the speed

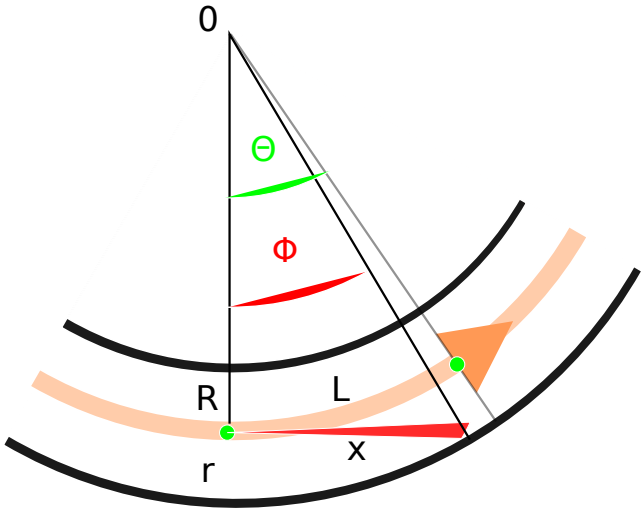

Figure 10: The path difference between protons (green) and photons(red). R and r are the bending and chamber radii, while L and x are respectively the paths the protons and the photons travel until the photon hits the chamber walls.

of light is assumed, therefore L and x are equally long by definition:

$$(R + r)^2 = R^2 + x^2 \tag{19}$$

$$x = \sqrt{2Rr + r^2} = 11.1 \text{ m} \tag{20}$$

$$\Phi = \tan^{-1} \frac{x}{R} \tag{21}$$

$$\Theta = \frac{L}{R} = \frac{x}{R} \tag{22}$$

$$\tag{23}$$

The time-delay between the beam and the synchrotron radiation is given by:

$$\Delta t = \frac{R(\Theta - \Psi)}{c} = 1.938 \cdot 10^{-13}\ s \tag{24}$$

This difference is negligible as it is much smaller than a time step of the simulation, which is normally around 10^{-11} s.

However, photons that are absorbed only after several reflections (note that the reflection coefficient for grazing incident photons on copper without sawtooth was measured to be larger than 80%) are delayed significantly with respect to the originating beam particle. One reflection to the opposite side of the chamber causes a delay of $\Delta t = \frac{2r}{c} = 1.48 \cdot 10^{-10}$ s, which is already longer than a time step in the simulations, but much shorter than the bunch spacing. Backward reflections, which are expected for sawtooth surfaces, lead to delays that can be of the order of the bunch spacing of 25 ns, for which a distance of travel of 7.5 m is required. This acts as an e-cloud seeding mechanism that extends to the bunch gaps, and could in principle alter the way the electron cloud decays.

To investigate the impact of the time structure of the photoelectron generation, a modified version of PyECLOUD

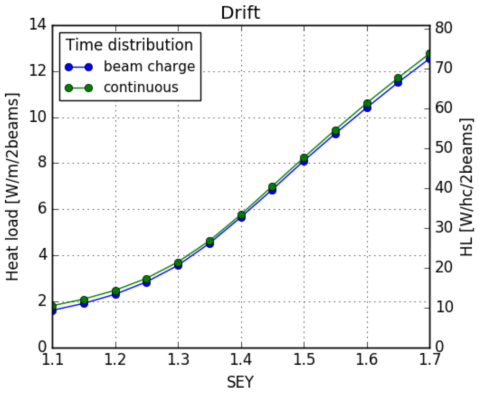

Figure 11: The effect of a generation of photoelectrons that is continuous in time is compared to the usual assumption, where the generation coincides with the beam charge profile. The case of a drift section is considered.

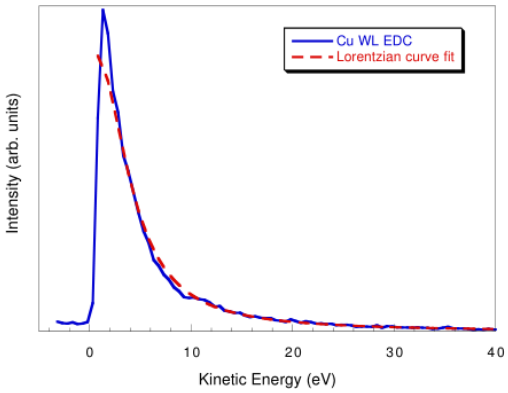

Figure 12: Photoemission spectra for 30 eV photons on copper together with Lorentzian fit to the low-dose WL spectrum centered at 0.64 eV and 3.7 eV wide [11].

has been utilized, in which photoelectrons are generated uniformly in time. The results for the case of a drift section are presented in Fig. 11 and compared to the usual PyECLOUD modeling. The heat loads are practically unaffected by the changes. Similar results are found also for the case of the dipole magnet. Therefore, changes to the code concerning the time structure of the emission are not deemed necessary.

Energy of generated photoelectrons

By default a truncated Gaussian is used for the energy distribution in PyECLOUD simulations. According to laboratory measurements [11], different distributions are more realistic (see Fig. 12). Therefore, other distributions have been optionally introduced in the simulation code. These are specified by the new input parameter **energy_distribution**, which allows to choose from the following options (see Fig. 13):

- a truncated Gaussian, which is the standard in PyECLOUD:

$$p(E) = \frac{1}{\sqrt{2\pi\sigma^2}}\, e^{-\frac{(E-\mu)^2}{2\sigma^2}} \tag{25}$$

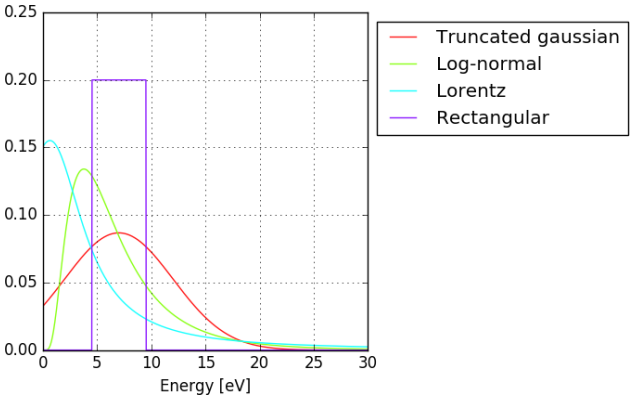

Figure 13: This plot shows a truncated normal distribution, as well as a log-normal distribution with the same mean and variance as the undistorted Gaussian distribution. In addition, also a Lorentzian and a rectangular distribution are shown.

- a Lorentzian, truncated to positive values as indicated by Fig. 12 (however it only fits well for the low-dose sample, otherwise the low-energy part is greatly reduced):

$$p(E) = \frac{1}{\pi} \frac{\sigma}{\sigma^2 + (E-\mu)^2} \tag{26}$$

- a log-normal distribution, which could probably also be fitted to the data in Fig. 12:

$$p(E) = \frac{1}{E\sigma\sqrt{2\pi}} e^{-\frac{(\ln E - \mu)^2}{2\sigma^2}} \tag{27}$$

  It shall be noted that μ and σ are simply parameters and not the mean and standard deviations of the distribution.

- a rectangular or a mono-energetic distribution (unphysical) for sensitivity studies.

Four different energy distributions shown in Fig. 13 were simulated. Figure 14 shows a comparison of the resulting e-cloud buildup. The simulations were performed with a generation of photoelectrons that is uniform in time. It is evident that the initial energy of the photoelectrons does not have any impact on the resulting heat loads.

SUMMARY

Electron cloud build-up simulations were performed for the main elements of the LHC arc half-cell (main dipoles and quadrupoles, corrector magnets, multipoles and drift spaces). Different assumptions on the photoelectron yield were made based on laboratory measurements of the LHC beam screen materials. Simulations performed with different models were compared against the simple case in which the e-cloud formation is seeded with a uniform initial electron distribution. The presence of photoelectrons has a significant impact on the e-cloud formation only in the cases of the drift spaces and of the dipole magnets. The effect of the photoelectrons

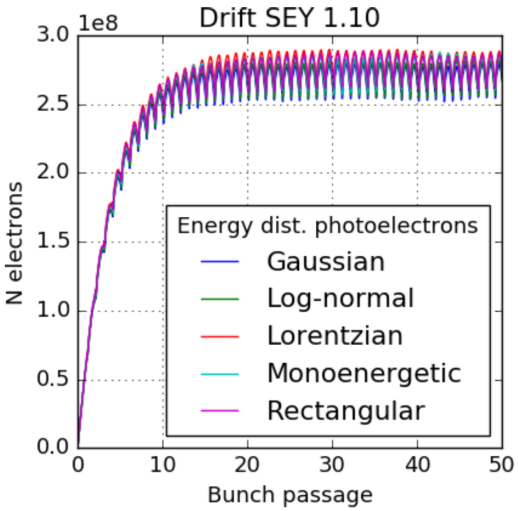

Figure 14: The impact of several different energy distributions of emitted photoelectrons is investigated by simulating a drift with different energy distribution functions.

is practically negligible for the quadrupoles and for higher order multipoles, in which the multipacting is stronger due to electrons trapped by the field gradient.

The simulation results were compared against measured heat load data from the LHC cryogenic system. Taking into account the effect of photoelectrons we can conclude that measurements for the cells with the lowest heat loads are compatible with a low SEY parameter (SEY<1.2, corresponding to a full surface conditioning).

The sensitivity of the simulation results on different characteristics of the photoemission process was also investigated. In particular we addressed the impact of the time structure of the photoemission production, and of the energy spectrum of the photoelectrons. None of these features was found to have a significant impact on the e-cloud buildup and, in particular, on the estimated heat loads.

ACKNOWLEDGEMENTS

The authors would like to thank G. Arduini, V. Baglin, O. Boine-Frankenheim, B. Bradu, E. Métral, A. Perin and A. Romano for their important input and support to the presented work.

REFERENCES

[1] G. Rumolo, F. Ruggiero, and F. Zimmermann, "Simulation of the electron-cloud build up and its consequences on heat load, beam stability, and diagnostics," *Physical Review Special Topics-Accelerators and Beams*, vol. 4, no. 1, p. 012801, 2001.

[2] L. Mether, "Electron cloud in 2016: cloudy or clear?," in *Proc. of the 7th Evian Workshop, Evian 13-15 Dec 2016*, 2016. `https://indico.cern.ch/event/578001/`.

[3] G. Iadarola, L. Mether, and G. Rumolo, "Filling schemes and e-cloud contraints for 2017," in *7th Evian Workshop on LHC beam operation*, pp. 239–244, 2017.

[4] G. Rumolo *et al.*, "Electron Cloud Effects at the LHC and LHC Injectors," in *Proc. of International Particle Accelerator Conference (IPAC'17), Copenhagen, Denmark*, May 2017.

[5] G. Apollinari, I. B. Alonso, O. Brüning, M. Lamont, and L. Rossi, *High-Luminosity Large Hadron Collider (HL-LHC)*. Geneva: CERN, 2015. Preliminary Design Report.

[6] G. Iadarola, *Electron Cloud studies for CERN particle accelerators and simulation code development*. PhD thesis, University of Naples Federico II, 2014.

[7] G. Iadarola, E. Belli, K. Li, L. Mether, A. Romano, and G. Rumolo, "Evolution of Python Tools for the Simulation of Electron Cloud Effects," in *Proc. of International Particle Accelerator Conference (IPAC'17), Copenhagen, Denmark, May, 2017*, JACoW.

[8] V. Baglin, I. R. Collins, and O. Gröbner, "Photoelectron yield and photon reflectivity from candidate LHC vacuum chamber materials with implications to the vacuum chamber design," in *Particle accelerator. Proceedings, 6th European conference, EPAC'98, 1998.*, 1998.

[9] V. Baglin, I. R. Collins, O. Gröbner, C. Grünhagel, B. Henrist, N. Hilleret, and B. Jenninger, "Measurements At EPA Of Vacuum And Electron-Cloud Related Effects," in *11th Chamonix - LHC Workshop*, 2001.

[10] N. Mahne, V. Baglin, I. Collins, A. Giglia, L. Pasquali, M. Pedio, S. Nannarone, and R. Cimino, "Photon reflectivity distributions from the LHC beam screen and their implications on the arc beam vacuum system," *Applied Surface Science*, vol. 235, no. 1–2, pp. 221 – 226, 2004. 8th European Vacuum Conference and 2nd Annual Conference of the German Vacuum Society.

[11] R. Cimino, V. Baglin, and I. Collins, "VUV synchrotron radiation studies of candidate LHC vacuum chamber materials," *Vacuum*, vol. 53, no. 1, pp. 273 – 276, 1999.

[12] P. Dijkstal, G. Iadarola, L. Mether, and G. Rumolo, "Simulation studies on the electron cloud build-up in the elements of the LHC Arcs at 6.5 TeV," tech. rep., Oct 2017.

[13] K. Jakobi, "Work function data: Datasheet from Landolt-Börnstein - Group III Condensed Matter · Volume 24B: "Electronic and Vibrational Properties" in SpringerMaterials."

[14] A. Hofmann, *The Physics of Synchrotron Radiation*. Cambridge: Cambridge University Press, 2004.

[15] E. Hatchadourian, P. Lebrun, and L. Tavian, "Supercritical Helium Cooling of the LHC Beam Screens," LHC Project Report 212, CERN, Geneva, 1998.

[16] O. Brüning, P. Collier, P. Lebrun, S. Myers, R. Ostojic, J. Poole, and P. Proudlock, *LHC Design Report*. Geneva: CERN, 2004.

[17] F. Zimmermann, "Electron-Cloud Effects in past and future machines - walk through 50 years of Electron-Cloud studies," in *Proceedings, 5th Workshop on Electron-Cloud Effects (ECLOUD'12): La Biodola, Isola d'Elba, Italy, June 5-9, 2012*, 2013.

[18] G. Iadarola, G. Rumolo and collaborators, "PyECLOUD Reference Manual." `https://github.com/PyCOMPLETE/PyECLOUD/wiki`.

[19] G. Iadarola, G. Rumolo, P. Dijkstal, and L. Mether, "Analysis of the beam induced heat loads on the LHC arc beam screens during Run 2," tech. rep., Dec 2017. `https://cds.cern.ch/record/2298915`.

[20] G. Iadarola, "Overview on heat loads in the LHC." These proceedings.